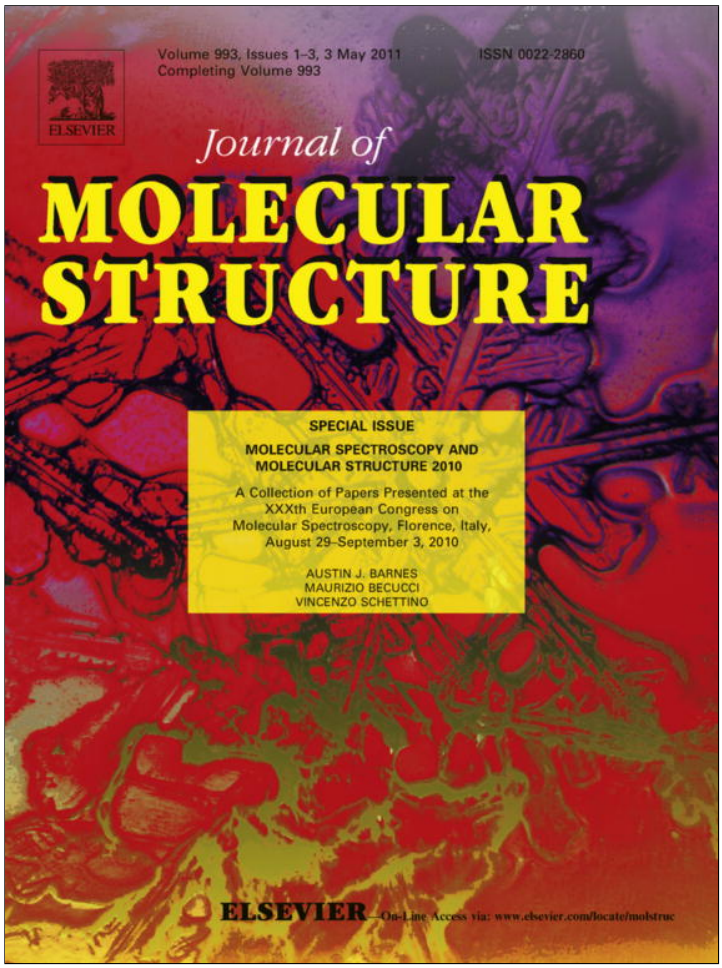

Journal of Molecular Structure 993 (2011) 167–176

Contents lists available at ScienceDirect

Journal of Molecular Structure

journal homepage: www.elsevier.com/locate/molstruc

Hydrothermal synthesis of α-Fe_2O_3 nanorings with the help of divalent metal cations, Mn^{2+}, Cu^{2+}, Zn^{2+} and Ni^{2+}

M. Gotić [a,*], G. Dražić [b], S. Musić [a]

[a] Ruđer Bošković Institute, Bijenička 54, HR-10002 Zagreb, Croatia
[b] Jožef Stefan Institute, Jamova 39, SI-1000 Ljubljana, Solvenia

ARTICLE INFO

Article history:
Available online 23 January 2011

Keywords:
Hematite
Alpha-Fe_2O_3
Phosphate
Nanorings
Divalent cations

ABSTRACT

The morphologies of α-Fe_2O_3 spindles and nanotubes was modified by the addition of divalent metal cations M^{2+} (M = Mn, Cu, Zn, Ni). Divalent metal cations gradually modify the spindle to pseudosphere and the nanotube to nanoring particle morphologies. At a higher concentration of added divalent cations the nanodisc morphology was obtained. The SEM/EDS and TEM/EDX analyses showed that precipitates contained Fe, O and P elements, but none of the precipitates contained divalent metal cations. The XRD patterns of each investigated sample fitted well to pure hematite (α-Fe_2O_3) and there were no other phases observed. The Mössbauer and XRD lines broadened with the addition of divalent metal cations. The mean crystallite sizes were calculated using the Scherrer equation from XRD line broadening of 104 and 110 lines of hematite. With the addition of a Mn^{2+} cation the mean crystallite size gradually increased in the *a*-axis direction. The relative high value of the mean crystallite size in the *a*-axis direction was found for nanorings modified by a Cu^{2+} cation. This high crystal distortion in the *a*-axis direction upon adding Cu^{2+} was explained by a strong Jahn–Teller effect of Cu^{2+} that has a tetragonally distorted coordination sphere in an octahedral coordination. Thus, quite opposite to a pure system, the modification by divalent metal cations induced the preferential growth of α-Fe_2O_3 crystals in the *a*-axis direction. It was suggested that divalent metal cations introduced the defects into the planes parallel to the basal plane (0 0 1) and thus changed the type of hydroxyl groups on hematite planes, which as a consequence switched the preferential growth of the α-Fe_2O_3 along the *c*-axis to the growth along the *a*-axis.

1. Introduction

There is a long tradition in the synthesis of iron oxide particles with tailored chemical composition, shape and size [1]. Moreover, this topic has recently expanded rapidly due to the application of iron oxide nanoparticles in biomedical research. In order to modify the shape of iron oxide particles a lot of different surfactants, organic molecules, cations and anions were used [1–4]. In particular, phosphate anions were often used to modify the shape of iron oxide particles [5–7]. For instance, Ozaki et al. [5] synthesized uniform spindle-shape colloidal hematite particles of narrow size distribution by the forced hydrolysis of ferric chloride solutions at an elevated temperature. It was shown that the concentration of phosphate ions had a significant effect on the axial ratio of hematite particles. Sugimoto et al. [6] synthesized monodispersed peanut-type hematite particles from condensed ferric hydroxide gel with the addition of phosphate. However, in spite of a long tradition in synthetic iron oxide chemistry a convenient and reproducible one-pot procedure for a large scale synthesis of iron oxide nanotubes and nanorings has been developed just recently by Jia et al. [8]. These authors have shown that phosphate anions can induce the preferential dissolution of the hematite spindle precursor to form single-crystalline iron oxide nanotubes. The same authors [9] introduced sulphate anions into the system in order to achieve a better control of its morphology and this double anion mediation resulted in the synthesis of iron oxide nanorings. However, despite a series of works using the etching process in an acid environment to produce hollow or nanotube morphology, it still remains a challenge for materials scientists to synthesize uniform nanorings using wet-chemistry methods. For instance, Luo et al. [10] synthesized single-crystal tetragonal α-MnO_2 nanotubes by hydrothermal treatment of $KMnO_4$ in a hydrochloric acid solution. Wang et al. [11] synthesized single-crystalline Cu_2O hollow nanocubes via a wet chemical route by means of a reducing (L-ascorbic acid) and simultaneously etching process with chloride ions in an acidic aqueous solution. Wang et al. [12] synthesized cobalt nanoskeletons with all six nanocube surfaces etching with fluoride ions. Lv et al. [13] prepared the spindle porous zerovalent iron (α-Fe) particles in two steps, first they synthesized the spindle-shape α-Fe_2O_3 via the Jia's procedure [8], then reduced the pre-synthe-

* Corresponding author.
E-mail address: gotic@irb.hr (M. Gotić).

0022-2860/$ - see front matter © 2011 Elsevier B.V. All rights reserved.
doi:10.1016/j.molstruc.2010.12.063

sized spindle-shape α-Fe_2O_3 particles by hydrogen gas. Fan et al. [14] modified the Jia's procedure [8] to synthesize ferrite MFe_2O_4 (M = Co, Mn, Ni, Cu) nanotubes. Hu et al. [15] modified the Jia's procedure [8] by introducing microwave radiation in the hydrothermal process.

Nanorings have also attracted a significant attention owing to their magnetic properties. The magnetic nanoring possesses the vortex state characterized by a magnetic moment circulating around the ring [8,16]. In such a state magnetization turns out of the plane at the very centre of the vortex structure. A magnetic vortex can store two bits of information by switching the vortex core polarization [17]. The magnetic properties of a nanoring are governed by its geometry rather than by intrinsic materials properties. α-Fe_2O_3 particles could be easily converted to ferrimagnetic Fe_3O_4 or γ-Fe_2O_3 particles under the hydrogen flow or in static hydrogen conditions at temperatures about 350 °C [18]. The morphology of α-Fe_2O_3 nanorings is perfectly preserved upon their conversion to Fe_3O_4 or γ-Fe_2O_3 [8,16].

In this work we successfully turn the α-Fe_2O_3 nanotube to nanoring morphology by modifying the hydrothermal method for obtaining α-Fe_2O_3 nanotubes, previously reported by Jia et al. [8,9]. In our modification we use the benefit of introducing divalent metal cations M^{2+} (M = Mn, Cu, Zn, Ni) into the system. With an increased M^{2+} addition the aspect ratio of iron oxide nanotubes gradually decreases and as a result α-Fe_2O_3 nanorings are formed. The formed α-Fe_2O_3 nanorings do not contain any trace of M^{2+} impurities, because upon exposure to hydrothermal and acidic conditions at temperatures above 220 °C divalent cations do not precipitate or adsorb on the α-Fe_2O_3 precipitate. It is suggested that the addition of divalent metal cations played an important role in changing the nanotube to nanoring morphology. However, quite opposite to a pure system where the crystal growth and dissolution of α-Fe_2O_3 along the *c*-axis was observed, the modification by divalent metal cations induced the preferential growth of α-Fe_2O_3 crystal grains along the *a*-axis.

2. Experimental

2.1. Chemicals

The chemicals $NH_4H_2PO_4$, $FeCl_3{\cdot}6H_2O$, $MnCl_2{\cdot}4H_2O$ and $ZnCl_2$ (anhydrous) supplied by *Kemika*, and $CuCl_2{\cdot}2\ H_2O$ and $NiCl_2{\cdot}6H_2O$ supplied by *Merck* were used. All chemicals were of analytical purity and used as obtained, without further purification. Double distilled water and absolute ethanol (*Kemika*) were also used.

2.2. Synthesis

α-Fe_2O_3 nanotubes and spindle-shaped nanoparticles were synthesized by hydrothermal treatment of a mixture of $FeCl_3$ and $NH_4H_2PO_4$ at 231 °C according to the Jia's procedure [8]. The experimental procedure was as follows: 3.2 mL of aqueous $FeCl_3$ solution (0.5 M) and 2.9 mL of aqueous $NH_4H_2PO_4$ solution (0.02 M) were mixed by stirring in a glass flask with a magnetic glass stirrer. Double distilled water was then added to the final volume of 80 mL. The mixture was stirred for 15 min, then transferred to two 50-mL Teflon-lined stainless steel autoclaves for hydrothermal treatment at 231 °C for 2 h (spindle-shaped nanoparticles) or 48 h (nanotube nanoparticles). The autoclaves were cooled down to room temperature, the precipitates were separated by centrifugation, rinsed with double distilled water and absolute ethanol, and dried overnight at 60 °C. In order to add two-valent cations to the system, 100 mL of 0.5 M aqueous solution of $FeCl_3$, $MnCl_2$, $ZnCl_2$, $CuCl_2$, and $NiCl_2$ were freshly prepared, then mixed by stirring in a predetermined volume using the glass flask and the magnetic stirrer with a glass envelope. For example, for 30 mol% of Mn^{2+} in solution, 30 mL of 0.5 M aqueous solution of $MnCl_2$ were added to 70 mL of the 0.5 M aqueous solution of $FeCl_3$, stirred for 15 min and then 6.4 mL of this solution (with $[Mn^{2+}]/[Fe^{3+}] + [Mn^{2+}] = 0.3$) was mixed with 5.8 mL of aqueous $NH_4H_2PO_4$ solution (0.02 M) following exactly the same procedure as described above for obtaining α-Fe_2O_3 nanotubes [8]. The concentration of Mn^{2+} was varied, whereas the concentrations of Cu^{2+}, Zn^{2+} and Ni^{2+} were fixed to 30 mol%, the concentration of nanoring formation. The experimental conditions for the synthesis of all samples are given in Table 1.

2.3. Characterization

X-ray diffraction (XRD) patterns were recorded at 20 °C using the APD 2000 X-ray powder diffractometer, with Cu Kα (λ = 1.54059 Å) radiation (40 kV and 30 mA conditions), graphite monochromator, NaI-Tl detector) manufactured by *ItalStructures*, Riva Del Garda, Italy. The XRD patterns were recorded over the 20–100° 2θ range with a 2θ step of 0.03° and a counting time per step of 9–13 s. The samples were mixed with Silicon paste P4 (*Wacker*) and put on XRD zero-quartz holder in the form of a thin layer.

The thermal field emission scanning electron microscope (FE-SEM), model JSM-7000F, manufactured by *Jeol Ltd.*, was connected to the EDS/INCA 350 (energy dispersive X-ray spectroscopy) manufactured by *Oxford Instruments Ltd*. In order to prevent the

Table 1
Experimental conditions for the hydrothermal synthesis of α-Fe_2O_3 nanoparticles of different morphologies.

Sample	$FeCl_3$ (mmol)	$NH_4H_2PO_4$ (mmol)	Molar ratio $[Fe^{3+}]/[PO_4^{3-}]$	$M^{2+}Cl_2$ (mmol)	M^{2+} (mol%)	Autoclaving at 231 °C (h)	Size (h/w) (nm/nm)	Aspect ratio (height/width)	α-Fe_2O_3 morphology
S0	1.60	0.0576	27.8	–	–	2	~380/~90	~4.2	Spindles
S1	1.44	0.0576	25.0	0.16 (Mn^{2+})	10	2	~320/~80	~4.0	Spindles
S2	1.28	0.0576	22.2	0.32 (Mn^{2+})	20	2	~200/~80	~2.5	Spindles
S3	1.12	0.0576	19.4	0.48 (Mn^{2+})	30	2	~94/~88	~1.1	Pseudospheres
S4	0.96	0.0576	16.7	0.64 (Mn^{2+})	40	2	~100	–	Ellipsoids, discs
S5	0.80	0.0576	13.9	0.80 (Mn^{2+})	50	2	~100	–	Ellipsoids, discs
S6	1.12	0.0576	19.4	0.48 (Mn^{2+})	30	6	~100	–	Nanorings, capsules
S7	1.12	0.0576	19.4	0.48 (Mn^{2+})	30	24	~110	–	Nanorings, capsules
S8	1.60	0.0576	27.8	–	–	48	~250/~100	~2.5	Nanotubes
S9	1.44	0.0576	25.0	0.16 (Mn^{2+})	10	48	~200/~80	~2.5	Nanotubes
S10	1.28	0.0576	22.2	0.32 (Mn^{2+})	20	48	~150/~100	~1.5	Nanotubes
S11	1.12	0.0576	19.4	0.48 (Mn^{2+})	30	48	~110	–	Nanorings
S12	0.96	0.0576	16.7	0.64 (Mn^{2+})	40	48	~110	–	Nanorings, discs
S13	0.80	0.0576	13.9	0.80 (Mn^{2+})	50	48	~110	–	Discs
S14	1.12	0.0576	19.4	0.48 (Cu^{2+})	30	48	~110	–	Nanorings
S15	1.12	0.0576	19.4	0.48 (Zn^{2+})	30	48	~110	–	Nanorings
S16	1.12	0.0576	19.4	0.48 (Ni^{2+})	30	48	~110	–	Nanorings

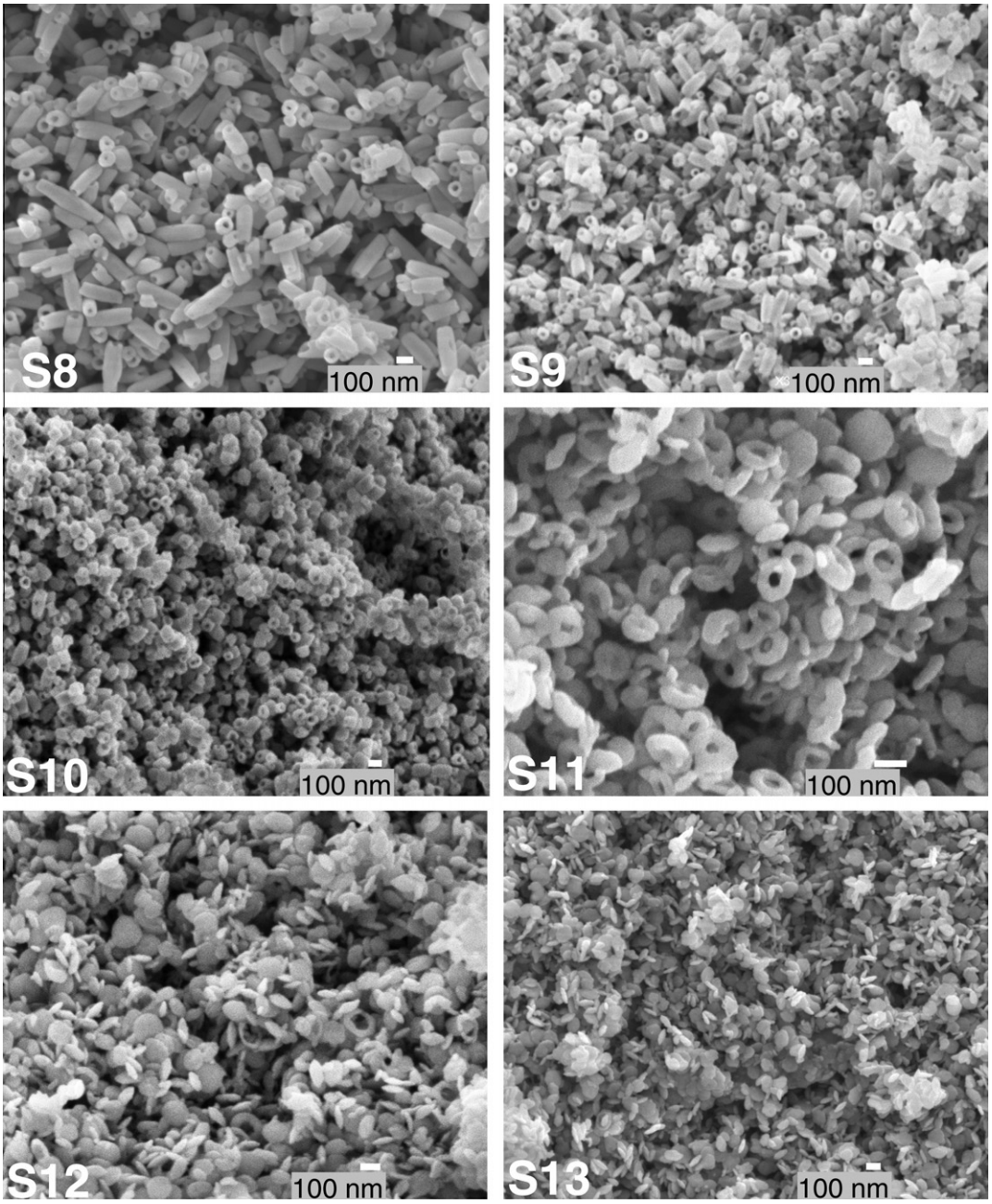

Fig. 1. SEM images of samples S8–S11 showing a change in nanotube morphology with the help of a Mn^{2+} cation. With the increase of Mn^{2+} in the aqueous precursor the original nanotube morphology (sample S8) continuously shortens (samples S9 and S10) and at 30 mol% of Mn^{2+} changes to a pure nanoring morphology (sample S11). At 40 mol% of Mn^{2+} in the aqueous precursor (sample S12) the particles precipitate in nanoring and disc morphologies. At the highest concentration of 50 mol% of Mn^{2+} in the aqueous precursor (sample S13) the nanoring morphology completely disappears and the particles appear only in disc morphology.

surface charging of some samples, a thin Au/Pd film was sputtered using Precision Etching Coating System, GATAN Model 682 equipped with a thickness monitor, GATAN Model 681.

A JEOL 2010F analytical electron microscope, equipped with a field-emission gun, was used for high-resolution transmission electron microscopy (HRTEM) investigations for all samples. The microscope was operated at 200 kV, and an energydispersive X-ray spectrometer (EDXS) LINK ISIS-300 from Oxford Instruments with an UTW Si–Li detector employed for the chemical analysis. The samples for TEM were prepared from a diluted suspension of nanoparticles in ethanol. A drop of the dispersion was placed on a holey carbon film deposited on a copper grid and left to dry at ambient temperature.

Table 2
Results of SEM/EDS quantitative analysis for element phosphor (P) found in selected samples.

Sample	P (mol%)
S8	0.73
S9	0.77
S10	0.92
S11	1.41
S12	1.51
S13	1.98

The ^{57}Fe Mössbauer spectra were recorded in the transmission mode using a standard instrumental configuration by *WissEl GmbH* (Starnberg, Germany). ^{57}Co in the rhodium matrix was used as a

Mössbauer source. The spectrometer was calibrated at 20 °C using the standard α-Fe foil spectrum. The velocity scale and all the data refer to the metallic α-Fe absorber at 20 °C. The experimentally observed Mössbauer spectra were fitted using the *MossWinn* program.

The Fourier transform infrared (FT-IR) spectra were recorded at 20 °C using a *Perkin–Elmer* spectrometer model 2000. The specimens were pressed into small discs using a spectroscopically pure KBr matrix. The spectra were recorded using a KBr beam splitter in the mid IR region (4000–400 cm^{-1}) and a Mylar beam splitter in the far IR region (700–200 cm^{-1}).

3. Results and discussion

Fig. 1 shows the SEM images of samples S8–S11. It illustrates the changing nanotube morphology as divalent cations are being added, in this case the Mn^{2+} cation. With an increase in Mn^{2+} in the aqueous precursor, the length of nanotubes (sample S8) continuously decreases (samples S9 and S10). At 30 mol% of Mn^{2+} nanotubes alter to nanoring morphology (sample S11). At 40 mol% of Mn^{2+} in the aqueous precursor (sample S12) the particles precipitate in nanoring and disc morphologies. At a concentration of 50 mol% of Mn^{2+} (sample S13) the nanoring morphology completely disappears and the particles appear only in disc morphology.

The determination of P in samples was performed using FE-SEM/EDS. These measurements of P were very accurate and reproducible. Table 2 sums up the results of SEM/EDS analysis for the element phosphorus. The elements Mn, Cu, Ni and Zn were not found in any of the samples, not even by PIXE or TEM/EDX analyses.

Fig. 2 shows the TEM images of samples S11, S14 and S15 obtained by a modification of the aqueous precursor by Mn^{2+}, Cu^{2+} or Zn^{2+} respectively. All the three divalent cations generated particles in the form of nanorings. On the shown TEM images one can see various contrasts thus enabling the volume estimation of nanorings.

Fig. 3a shows HRTEM image of sample S14. One can see on this figure the (1 1 1) crystal planes over the whole area in spite of the different contrasts, indicating that the nanoring is monocrystalline. Fig. 3b shows HRTEM image of sample S14 with a nanoring axis of [0 0 1]. On both HRTEM figures the clear lattice image with consistent lattice fringes through the whole area indicates the high crystallinity and monocrystalline nature of the α-Fe_2O_3 nanorings.

Fig. 4 shows the XRD powder diffraction patterns of samples S8 (nanotubes) and S14 (nanorings obtained by Cu^{2+} modification). All XRD peaks are indexed in accordance with a pure corundum structure, space group $R\bar{3}c$ (167) of hematite (ICDD card: 33-0664). The selected powder XRD patterns are typical of the sample investigated. The XRD patterns of all investigated samples fitted well to pure hematite. The other phases were not observed.

Fig. 5 shows two XRD lines of interest having Miller indices 104 and 110. The broadening of XRD lines is related to the average size and shape of crystals. The mean crystallite (crystal grain) size can be estimated on the basis of the Scherrer formula, which presupposes that the XRD line broadening is solely caused by the decreasing crystallite size [1]. The Scherrer formula gives the mean crystallite size perpendicular to a given plane *hkl* [1,19]. The full width at half maximum (FWHM) of the 104 and 110 lines and the calculated average crystallite sizes are given in Table 3. The FWHM of these lines was corrected for the instrumental line broadening. The width of the line 104 increases with the Mn addition, from 0.096 in the unmodified sample S8 to 0.238 2θ degrees in the highly modified sample S13. Since the plane 104 is related to the near basal plane (*a*-axis), the calculated mean crystallite size

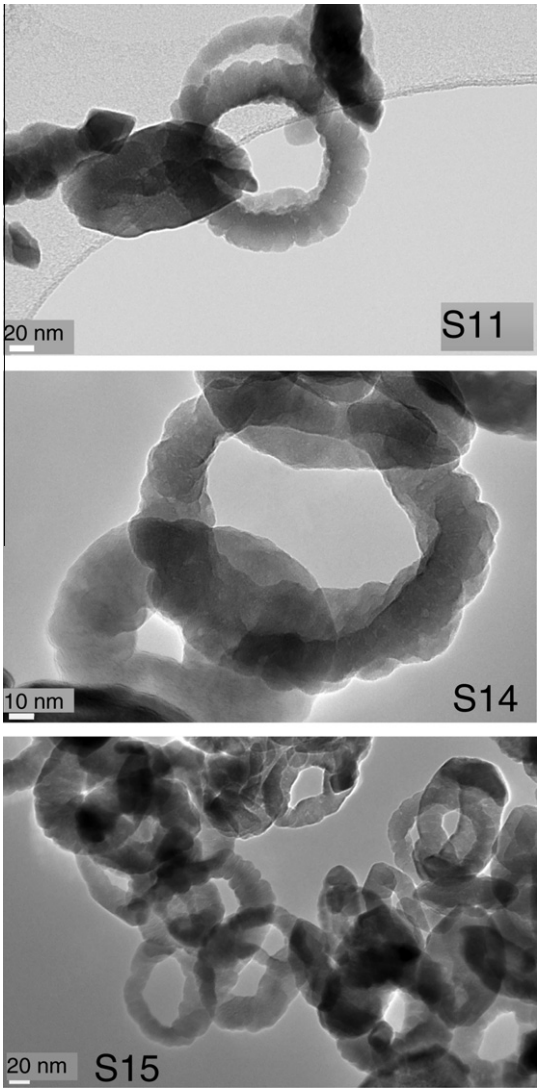

Fig. 2. TEM images of samples S11 (Mn^{2+}), S14 (Cu^{2+}) and S15 (Zn^{2+}). All the three divalent cations generated particles in the form of nanorings.

corresponds to the crystallite dimensions in the *c*-axis direction [1,20]. The narrower the 104 line, the more elongated the crystal along the *c*-axis. The opposite applies to the 110 plane: as the FWHM of the 110 line decreases, the crystal is longer (thicker) in the *a*-axis direction. The nanotubes grow along the *c*-axis and this accords with the narrow 104 and the broad 110 line. For nanodisc morphology (SEM image of sample S13, Fig. 1) the length of crystals in the *a*-axis direction is much greater than in the *c*-axis direction, which fits very well to the relatively broad 104 and the narrow 110 line. The width of the line 110 for nanorings obtained in the presence of Cu (sample S14) is significantly narrower than that of the nanorings obtained in the presence of its Mn counterpart (sample S11). This implies that the mean crystallite size in the *a*-axis direction is much greater for Cu-nanorings (significant elongation along the *a*-axis) in comparison with its Mn counterpart, and also that divalent cations play an active role in the modification of α-Fe_2O_3 morphology.

Fig. 6 shows the Mössbauer spectra of samples S8, S10 and S11. The Mössbauer spectrum of the unmodified sample S8 is fitted with one sextet. The Mössbauer spectra of the Mn^{2+}-modified samples S10 and S11 are fitted with two sextets due to the slightly broadened Mössbauer lines. The modification of the aqueous precursor by Cu^{2+} Zn^{2+} and Ni^{2+} also broadened the Mössbauer hema-

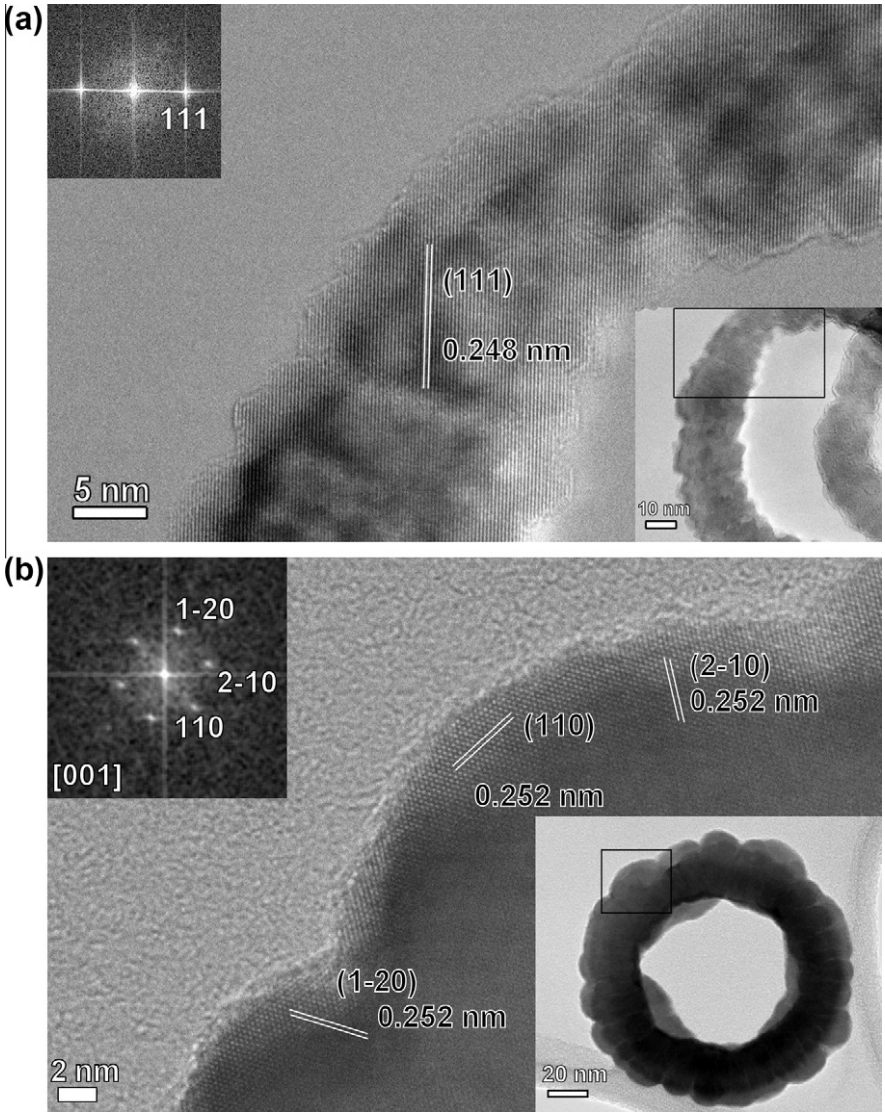

Fig. 3. (a) HRTEM image of sample S14 (inset right bottom) where (1 1 1) crystal planes are observed over the entire area, indicating that the nanoring is monocrystalline. The nanoring is not in the exact low-zone axis orientation, so just fringes of one planes are visible (left top inset is FFT of the HRTEM image). Note (1 1 1) facetting at inner and outer ring surfaces; (b) HRTEM image of sample S14 and indexed FFT (inset left top) indicating that the nanoring is monocrystalline and in [0 0 1] zone axis.

tite lines. The Mössbauer parameters are given in Table 4. The coupling between the primary α-Fe_2O_3 particles as well as introducing the defects into the α-Fe_2O_3 crystal grains may cause a reduction in the hyperfine magnetic field and a broadening of Mössbauer lines.

Fig. 7 shows the FT-IR spectra of samples S0–S5. The spectra were recorded using the KBr beam splitter in the mid IR region from 4000 to 400 cm^{-1}. The characteristic region between 2000 and 400 cm^{-1} is shown. The IR bands at 1163, 1074, 1039, 1007, 972 and 935 cm^{-1} are due to a specifically adsorbed phosphate in the form of both monodentate and bidentate surface complexes. Both complexes could be protonated in low pH conditions associated with hydrothermal synthesis examined in this work ($pH \leqslant 2$). The relative intensities of phosphate bands increase from sample S0 to S5, which is in accordance with SEM/EDS analysis Table 2). The strong IR bands from 800 to 400 cm^{-1} correspond to the hematite lattice vibration. Hematite has six IR active modes, two A_{2u} modes with polarization parallel to the hexagonal *c*-axis (symbol || in Fig. 5) and four E_u modes with polarization perpendicular to the hexagonal *c*-axis (symbol $\perp$ in Fig. 5). For that reason the position and intensities of IR bands are sensitive to particle size and morphology [21–25]. Due to a high aspect ratio, the || and $\perp$ modes at 584 and 537 cm^{-1} respectively in sample S0 are fully resolved. With the decrease in the nanoparticle aspect ratio the || mode shifts significantly to higher wavenumbers and the $\perp$ mode shifts slightly to lower wavenumbers. Accordingly, these two bands overlap into one IR band at 565 cm^{-1} (sample S3). Samples S4 and S5 have quite a different morphology (discs) in comparison with samples S0–S3 (spindles to pseudosphere). The disc morphology is more comparable to a plate-like morphology. The IR position and relative intensity of || and $\perp$ modes for plate-like morphologies differ from those of the spindles. Rendon and Serna [21] assigned IR bands at 650 and 400 cm^{-1} in irregular lath-shaped hematite particles to || mode and IR bands at 525, 440, 300 and 230 cm^{-1} to $\perp$ mode. Blanchard et al. [25] computed the IR spectrum of hematite using *ab initio* quantum mechanical calculations. The computed IR spectra for platy, spherical and ellipsoidal particles with a different aspect ratio showed a qualitative agreement with experimental observations. In accordance with the theoretical hematite spectra computed by Blanchard et al. [25] and the results of Serna et al. [22], the IR bands for samples S4 and S5 at 541 or 544 cm^{-1} are assigned to the $\perp$ mode, whereas the IR band at 629 cm^{-1} is assigned to the || mode.

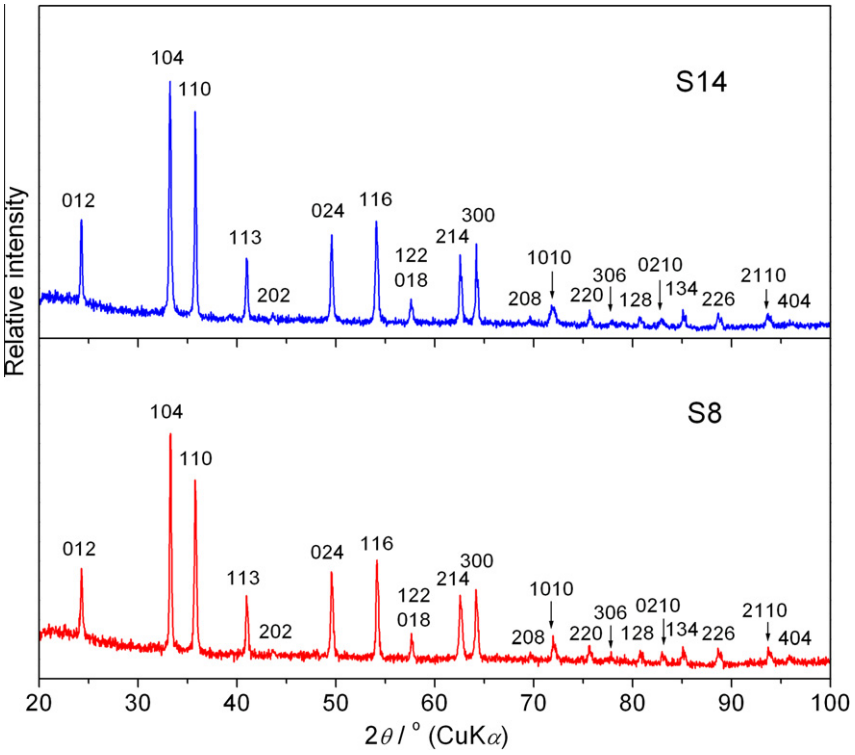

Fig. 4. XRD powder diffraction patterns of samples S8 (nanotubes) and S14 (nanorings obtained by Cu^{2+} modification). All XRD peaks are indexed in accordance with a pure corundum structure (space group $R\bar{3}c$) of hematite (ICDD card No.: 33-0664).

Fig. 8 shows the FT-IR spectra and corresponding SEM images of samples S0, S1, S2, S3 and S5 in the far IR region from 700 to 200 cm^{-1} (Mylar beam splitter). This figure gives a better demonstration of the morphology effect on the FT-IR spectra of α-Fe_2O_3 nanoparticles.

Fig. 9 shows three basic morphologies considered in this work. α-Fe_2O_3 in nanotube morphology was hydrothermally synthesized first by Jia et al. [8] at a Fe^{3+}/PO_4^{3-} molar ratio of 27.8. In order to better control the morphology of α-Fe_2O_3 nanoparticles, the same authors introduced the sulphate anion into the system and as a result nanorings were obtained [9]. Hu et al. [15] introduced microwave synthesis, whereas Fan et al. [26] adjusted the molar ratio Fe^{3+}/PO_4^{3-} to ~7 in order to obtain the nanoring morphology. In this work the divalent metal cations were introduced into the precipitation system in order to better control the particle morphology. The divalent metal cations used without exception at a concentration of 30 mol% alter the spindles to pseudospherical particles and nanotubes to nanorings. Unlike the sulphate anion, the divalent cations do not adsorb on the α-Fe_2O_3 precipitate at a pH below 3. With the increase in the divalent cations in the aqueous precursor the $[Fe^{3+}]/[PO_4^{3-}]$ ratio decreases. One can argue that the change in morphology is due to a decrease in the $[Fe^{3+}]/[PO_4^{3-}]$ ratio and that added divalent cations produce no effect. However, upon the addition of 30 mol% of divalent metal cations to the system, the $[Fe^{3+}]/[PO_4^{3-}]$ ratio is 19.4, which is much above the ratio ($[Fe^{3+}]/[PO_4^{3-}]$ of about seven at which nanorings are formed in a pure system, as reported by Fan et al. [26]. Furthermore, the introduction of divalent cations broadened the XRD and Mössbauer lines, whereas the sulphate anion had no effect on the XRD patterns and Mössbauer spectra [9]. Moreover, the values of the mean crystallite size in the *a*-axis direction determined from the broadening of the line 110 using the Scherrer equation for nanorings obtained in the presence of Cu^{2+} ions (sample S14) are significantly higher in comparison with the values obtained in the presence of its Mn counterpart (Table 3, sample S11). This means that divalent cations play an active role in the modification of α-Fe_2O_3 morphology. The SEM/EDS and TEM/EDX analyses showed that precipitates did not contain divalent metal cations. However, it is quite possible that modified samples contains less than 0.1 mol% of divalent metal cations in α-Fe_2O_3 structure, because this is below the detection limits of TEM/EDS technique. This very small quantity of divalent metal cation can produce a lot of defects in α-Fe_2O_3 structure, because of Avogadro constant, and this in turn reflects on Mössbauer spectra. The results reported by Kandori et al. [27–29] also confirmed the influence of metal cations on the morphology and structure of hematite produced from a forced hydrolysis reaction in $FeCl_3$–HCl aqueous solutions.

The role of divalent cations in tuning the aspect ratio of α-Fe_2O_3 particles could be assumed to be as follows: at room temperature and pH ⩽ 2 both cations Fe^{3+} and M^{2+} are highly soluble in an aqueous solution and surrounded more or less equally by Cl^- and $H_2PO_4^-$ anions. $H_2PO_4^-$ is the predominant charged phosphate species in an aqueous solution at pH ⩽ 2. Upon autoclaving at an elevated temperature the Fe(III) forced hydrolysis proceeded by the formation of monomers $[Fe(OH)]^{2+}$ and dimmers $([Fe_2(OH)_2]^{4+}$, followed by the formation of bigger positively charged polynuclear (PN) species. Chloride anions (Cl^-), unlike NO^{3-} anions [30], incorporate into PNs thus neutralizing their positive charge, so that these electrically neutral and low molecular weight PN species coagulate and easily agglomerate to produce a kinetically favourable oxyhydroxide intermediate phase (not found in this work). It is well documented that an oxyhydroxide intermediate phase transforms to α-Fe_2O_3 by the dissolution/recrystallisation mechanism [31–33]. Upon hydrothermal synthesis from $FeCl_3$ acidic aqueous solution without the presence of phosphate α-Fe_2O_3 precipitated in the form of equiaxed particles, e.g., in the form of spherical or rhombohedral particles. With the addition of phosphate to the same system, the elongated spindle-shaped particles

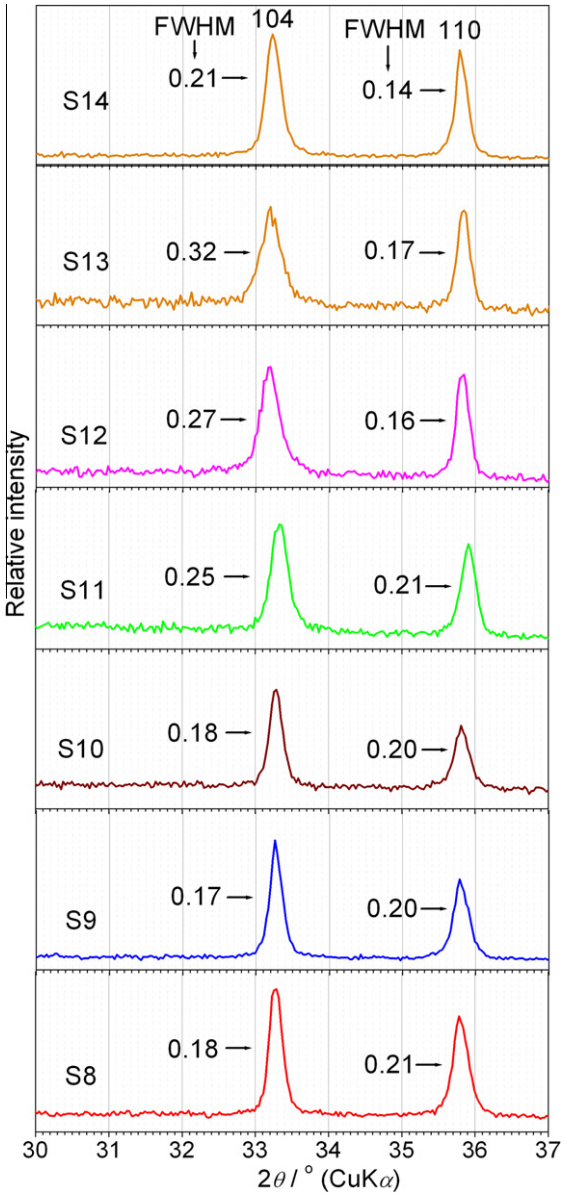

Fig. 5. XRD powder diffraction patterns of samples S8 to S13 (nanotubes to nanodiscs) showing the region of two hematite lines with Miller indices 104 and 110.

Table 3
The values of full width at half maximum (FWHM) for 104 and 110 XRD lines of hematite (α-Fe_2O_3), corrected for instrumental broadening. The mean crystallite (crystal grains) size perpendicular to the 104 plane along the near *c*-axis (D_{104}) and the mean crystallite size in the *a*-axis direction (D_{110}), were calculated using the Scherrer formula ($D_{hkl} = 0.94\lambda/\beta \cos\theta$ where λ is the X-ray wave length, β the full width of the diffraction line at one half of the maximum intensity and θ the Bragg angle). The ratio D_{104}/D_{110} is an estimation of the crystallite aspect ratio.

Sample	FWHM[a] 104	FWHM[a] 110	D_{104} (nm)	D_{110} (nm)	D_{104}/D_{110}
S8	0.12	0.15	72	58	1.24
S9	0.11	0.14	79	62	1.27
S10	0.12	0.14	72	62	1.16
S11	0,20	0.15	43	58	0.74
S12	0.22	0.09	39	97	0.40
S13	0.28	0.11	31	79	0.39
S14	0.15	0.07	58	125	0.46

[a] The corrected FWHM values are presented, which are obtained from the plot for the corrections of the observed diffraction profile for instrumental broadening.

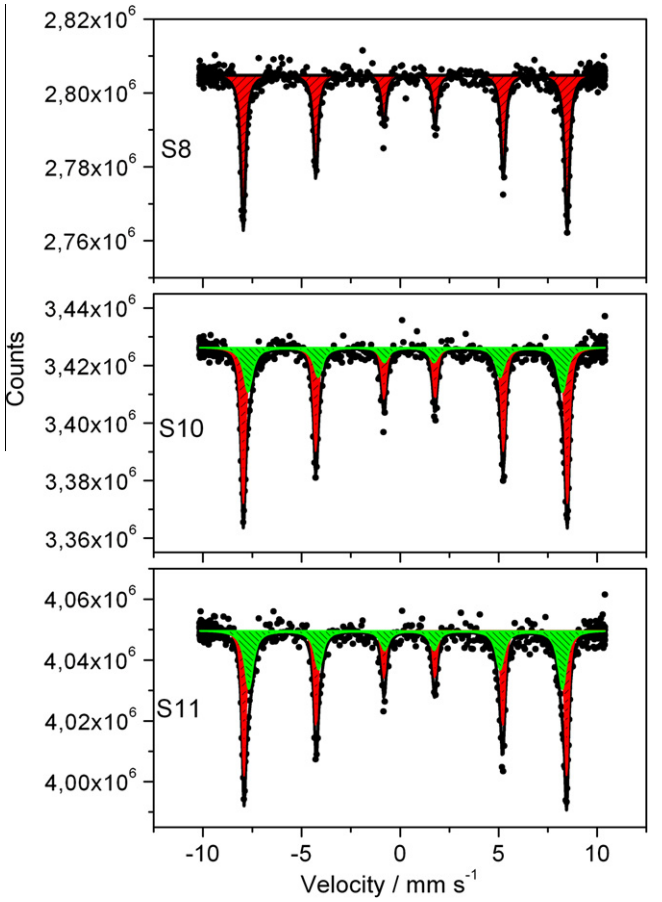

Fig. 6. Mössbauer spectra of samples S8, S10 and S11 recorded at 20 °C. The Mössbauer spectrum of unmodified sample S8 is fitted with one sextet. The Mössbauer spectra of modified samples S10 and S11 are fitted with two sextets due to slightly broadened Mössbauer lines. Mössbauer parameters are given in Table 2.

precipitated due to the selective adsorption of phosphate ions on the surfaces parallel to the *c*-axis in hematite (Fig. 9, left). Jia et al. [8,9] explained the selective adsorption of phosphate by the high adsorption capacities and affinities for phosphate to hematite for planes parallel to the *c*-axis. The planes parallel to the *c*-axis have single coordinated surface hydroxyl groups, which are responsible for high capacities and preferential adsorption as well as dissolution of Fe^{3+} along the *c*-axis. On the other hand, the basal plane (0 0 1) that has doubly coordinated hydroxyl groups is virtually inactive to phosphate adsorption. Almeida et al. [31–33] suggest that the phosphate ions are adsorbed preferentially on faces parallel to the *c*-axis of α-Fe_2O_3 because of the better matching of O–O interatomic distance of PO_4^{3-} anions (2.5 Å) with the Fe–Fe spacing parallel (2.88 Å) rather than perpendicular (5.02 Å) to the *c*-axis. Both explanations are complementary and satisfactorily explain the preferential growth of α-Fe_2O_3 particles along the *c*-axis in the presence of phosphate. However, in the presence of divalent cations in an early stage of reaction divalent metal cations can form surface complexes with hydroxyl groups of polynuclear complex (PN). Such mono- and binuclear complexes involve the coordination of metal cations and release the protons from the surface as proposed by Kandori et al. [27–29]:

$$(PN)Fe^{III}\text{—}OH + M^{2+} \rightarrow (PN)Fe^{III}\text{—}OM^{2+} + H^{+} \quad (1)$$

There is also a possibility that surface binuclear bidentate complexes are formed:

$$2(PN\text{—}OH) + M^{2+} \rightarrow (PN\text{—}O)_2M + 2H^{+} \quad (2)$$

Table 4
^{57}Fe Mössbauer parameters at 20 °C calculated for selected samples using the MossWinn program.

Sample	Sextet	IS (mm s^{-1})	QS (mm s^{-1})	B_{hf} (T)	LW (mm s^{-1})	Relative area A (%)	Phase composition	*Chi*
S8	H1	0.37	−0.22	51.0	0.30	100	α-Fe_2O_3	1.36
S10	H1	0.37	−0.21	51.0	0.26	62.7	α-Fe_2O_3	1.64
	H2	0.36	−0.20	49.5	0.55	37.3		
S11	H1	0.37	−0.21	50.8	0.24	54.0	α-Fe_2O_3	1.78
	H2	0.38	−0.19	49.3	0.51	37.3		
S14	H1	0.37	−0.20	51.2	0.26	63.6	α-Fe_2O_3	1.77
	H2	0.37	−0.20	49.6	0.45	36.4		
S15	H1	0.37	−0.21	51.1	0.26	61.7	α-Fe_2O_3	1.21
	H2	0.38	−0.23	49.5	0.54	38.3		
S16	H1	0.37	−0.21	51.2	0.25	56.4	α-Fe_2O_3	1.66
	H2	0.36	−0.20	49.7	0.49	43.6		

Key: IS = isomer shift given relative to α-Fe at 20 °C; QS = quadrupole shift; B_{hf} = hyperfine magnetic field; LW = line width; Chi = goodness of fitting (1.00 = relatively very good fitting; 2.00 = relatively weak fitting).
Error: IS = ±0.01 mm s^{-1}; QS = ±0.01 mm s^{-1}; B_{hf} = ±0.2 T.
Remarks: H1 = sextet of hematite; H2 = sextet introduced due to broadness of lines.

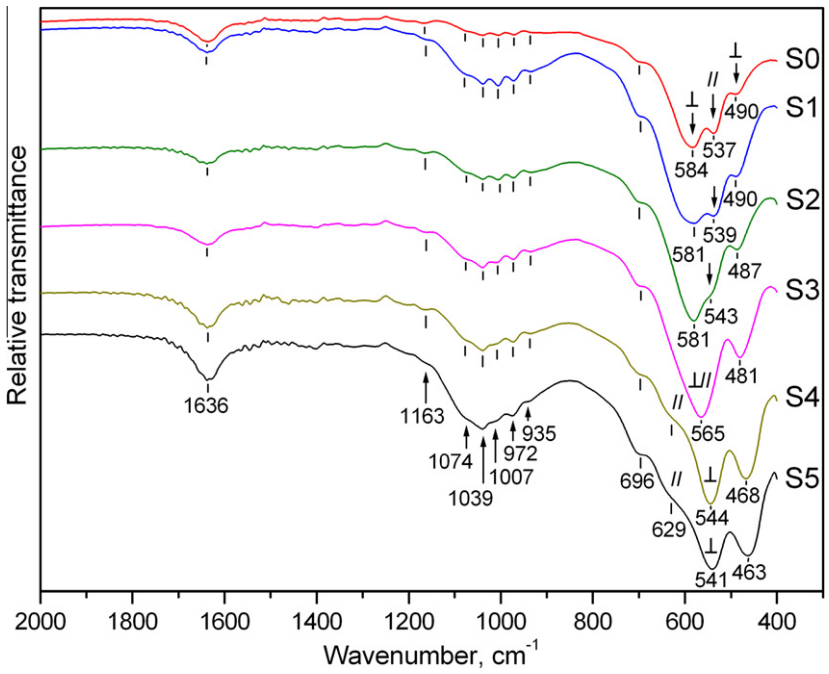

Fig. 7. FT-IR spectra of samples S0–S5. The spectra were recorded using the KBr beam splitter in the mid IR region from 4000 to 400 cm^{-1}. The characteristic region between 2000 and 400 cm^{-1} is shown. Symbols ⊥ and || indicate the IR mode perpendicular (E_u) and parallel (A_{2u}) to the *c*-axis direction.

where M = Mn^{2+}, Cu^{2+}, Zn^{2+} and Ni^{2+}.

These surface complexes, i.e., PN species with incorporated divalent metal cations are building blocks for the precipitation of kinetically more favourable oxyhydroxide primary particles. In this work we do not analyse the precipitate in an early stage of synthesis and hence we found no oxyhydroxide primary particles in our samples. When metastable oxyhydroxide primary particles grow to some critical size they start to dissolve, thus supplying the Fe^{3+} for α-Fe_2O_3 nucleation.

The experimental results undoubtedly showed the influence of M^{2+} cations on changes in the morphology of α-Fe_2O_3 particles. This process started with nucleation and was followed by the crystal growth of α-Fe_2O_3. In spite of the fact that the actual mechanism of nanoring formation in the present work cannot be identified with certainty, it can be suggested that surface interactions between M^{2+} cations and phosphates and specific α-Fe_2O_3 planes (starting with nucleation) play an important role in the changing of α-Fe_2O_3 nanotube to nanoring morphology. Likewise, the fact is the absence of M^{2+} cations in α-Fe_2O_3 particles. However, the microstructural changes resulting from the presence of M^{2+} cations during the synthesis of α-Fe_2O_3 nanorings were clearly evidenced by experimental techniques used in this work. Besides, the change of the preferential crystallite growth from occurring along the *c*-axis for a pure system to along the *a*-axis for samples modified by M^{2+} cations was determined using the Scherrer equation from the diffraction line broadening of 104 and 110 lines of α-Fe_2O_3. The mean crystallite size gradually increased in the *a*-axis direction with the addition of Mn^{2+} cations. The highest value of the mean crystallite size in the *a*-axis direction was found for nanorings modified by a Cu^{2+} cation. This high crystal distortion in the *a*-axis direction upon adding Cu^{2+} can be explained by a strong Jahn–Teller effect of Cu^{2+} that has a tetragonally distorted coordination sphere in an octahedral coordination [27–29]. It can be inferred that divalent metal cations brought defects into the planes

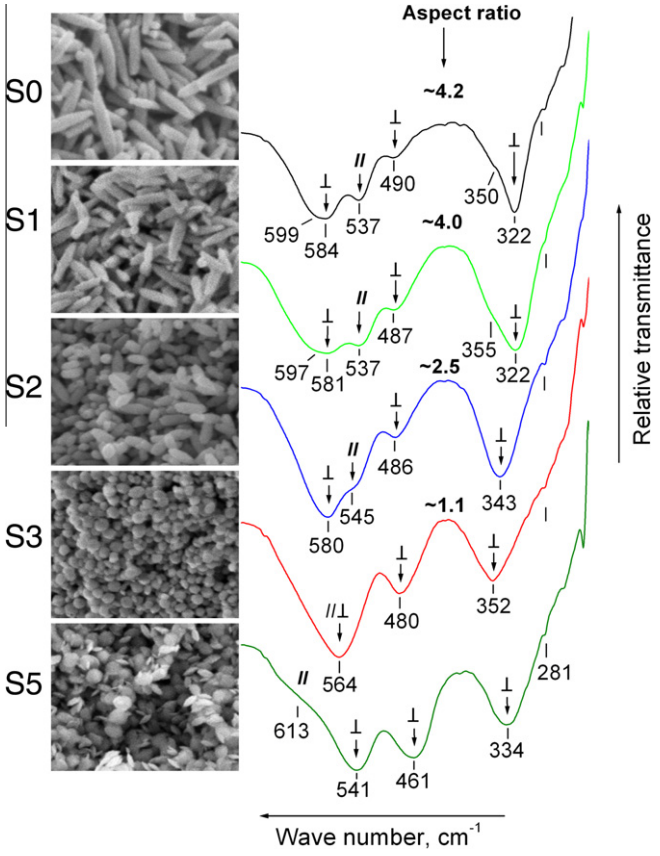

Fig. 8. FT-IR spectra and corresponding SEM images of samples S0, S1, S2, S3 and S5. The spectra were recorded using a Mylar beam splitter in the far IR region from 700 to 200 cm^{-1}. This figure is an illustration of the aspect ratio effect on the FT-IR spectra of α-Fe_2O_3 nanoparticles. The aspect ratios continuously decrease from ~4.5 for spindle to ~1.1 for pseudospherical nanoparticles. Symbols $\perp$ and || indicate the IR mode perpendicular (E_u) and parallel (A_{2u}) to the *c*-axis direction.

parallel to the basal plane (0 0 1), thus changing the type and coordination of hydroxyl groups on hematite planes, which as a consequence switched the preferential growth of the α-Fe_2O_3 crystal grains along the *c*-axis to that along the *a*-axis.

4. Conclusion

It has been shown that the addition of divalent metal cations has a strong impact on the morphology and orientation of α-Fe_2O_3 crystal growth and dissolution. The addition of divalent metal cations gradually modified the spindle to pseudosphere and nanotube to nanoring particle morphologies. At a higher concentration of added divalent cations the nanodisc morphology was obtained.

The SEM/EDS and TEM/EDX analyses showed that the precipitates contained elements Fe, O and P, but none of the precipitates contained any of the divalent cations.

The developing α-Fe_2O_3 particle morphologies were clearly demonstrated by FT-IR spectroscopy. It was found that the position and intensities of IR bands depended strongly on the α-Fe_2O_3 particle morphologies. The α-Fe_2O_3 particles with a high aspect ratio had fully resolved A_{2u} (||) and E_u ($\perp$) modes at 584 and 537 cm^{-1}, respectively.

The Mössbauer and XRD lines broadened with an increasing M^{2+} addition. The XRD line broadening of 104 and 110 lines shows a change in the crystallite size and shape of α-Fe_2O_3. The mean crystallite size gradually increased in the *a*-axis direction with the addition of Mn^{2+} cations. The highest value of the mean crystallite size in the *a*-axis direction showed the nanorings modified by 30 mol% of Cu^{2+} cations. This high crystal distortion in the *a*-axis direction upon the addition of Cu^{2+} could be attributed to a strong Jahn–Teller effect of Cu^{2+} that has a tetragonally distorted coordination sphere in an octahedral coordination.

Quite opposite to a pure system the divalent metal cations induced the preferential growth of α-Fe_2O_3 crystal grains in the *a*-axis direction. It was suggested that divalent cations introduced

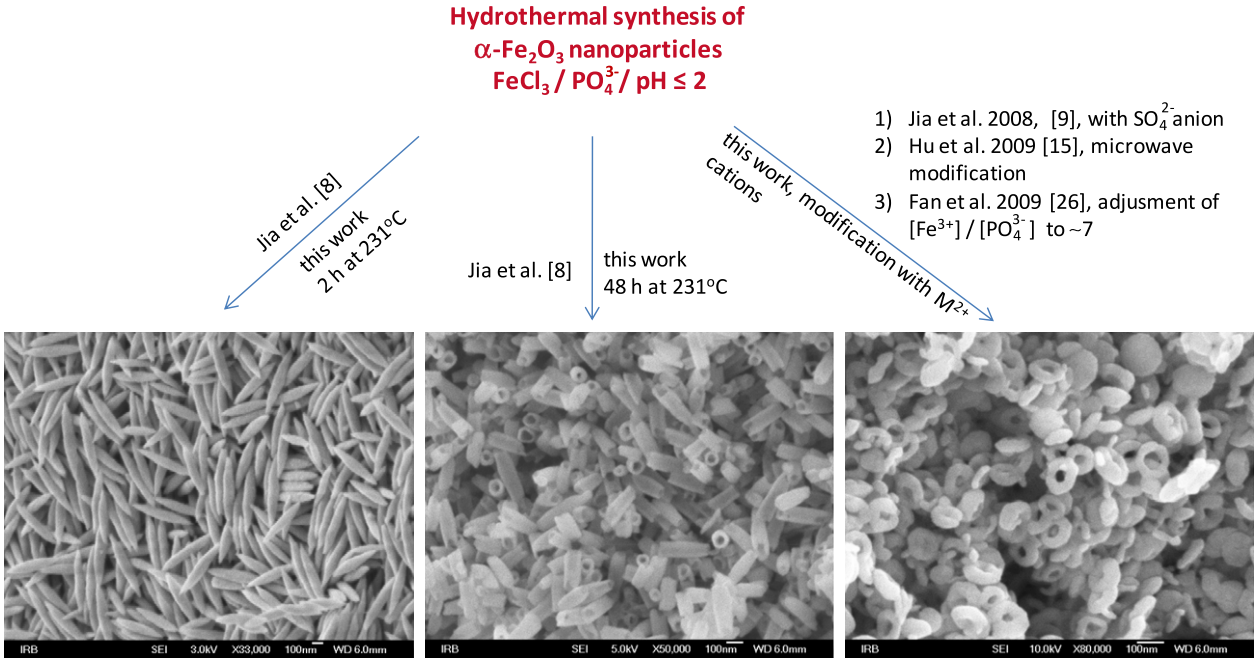

Fig. 9. SEM images of three basic morphologies important for this work. The α-Fe_2O_3 in nanotube morphology was hydrothermally synthesized first by Jia et al. [8]. The same authors introduced modification by a sulphate anion to obtain nanorings [9]. Hu et al. [15] introduced microwave synthesis, whereas Fan et al. adjusted the molar ratio of Fe^{3+}/PO_4^{3-} to ~7 in order to obtain the nanoring morphology. In this work the modification by divalent metal cations was introduced in order to obtain nanorings and to better control the particle morphology.

the defects into the planes parallel to the basal plane (0 0 1), thus changing the type of hydroxyl groups on hematite planes, which in turn switched the preferential growth of α-Fe_2O_3 along the *c*-axis to the growth along the *a*-axis.

The modification by divalent metal cations could be used as a general approach to the control of nanoparticle morphology using forced hydrolysis in highly acidic aqueous solutions without producing any changes in the chemical and phase composition of the product.

Acknowledgments

The authors thank Dr. Stjepko Krehula, Prof. Stanko Popović and Dr. Mira Ristić for valuable discussion. Also, the authors wish to thank Mr. Jasmin Forić for help in experimental work.

References

[1] R.M. Cornell, U. Schwertmann, The Iron Oxides: Structure, Properties, Reactions, Occurrences and Uses, second ed., Wiley-VCH Verlag GmbH & Co. KgaA, Weinheim, 2003.
[2] S. Musić, M. Gotić, N. Ljubešić, Mater. Lett. 25 (1995) 69.
[3] M. Gotić, S. Popović, N. Ljubešić, S. Musić, J. Mater. Sci. 29 (1994) 2474.
[4] S. Krehula, S. Musić, Mater. Chem. Phys. 123 (2010) 67.
[5] M. Ozaki, S. Kratohvil, E. Matijević, J. Colloid Interf. Sci. 102 (1984) 146.
[6] T. Sugimoto, M.M. Khan, A. Muramatsu, Colloids Surf. A 70 (1993) 167.
[7] M. Gotić, S. Musić, S. Popović, L. Sekovanić, Croat. Chem. Acta 81 (2008) 569.
[8] C.-J. Jia, L.-D. Sun, Z.-G. Yan, L.-P. You, F. Luo, X.-D. Han, Y.-C. Pang, Z. Zhang, C.-H. Yan, Angew. Chem. Int. Ed. 44 (2005) 4328.
[9] C.-J. Jia, L.-D. Sun, F. Luo, X.-D. Han, L.J. Heyderman, Z.-G. Yan, C.-H. Yan, K. Zheng, Z. Zhang, M. Takano, N. Hayashi, M. Eltschka, M. Kläui, U. Rüdiger, T. Kasama, L. Cervera-Gontard, R.E. Dunin-Borkowski, G. Tzvetkov, J. Raabe, J. Am. Chem. Soc. 130 (2008) 16968.
[10] J. Luo, H.T. Zhu, H.M. Fan, J.K. Liang, H.L. Shi, G.H. Rao, J.B. Li, Z.-M. Du, Z.X. Shen, J. Phys. Chem. C 112 (2008) 12594.
[11] Z. Wang, H. Wang, L. Wang, L. Pan, J. Phys. Chem. Solids 70 (2009) 719.
[12] X. Wang, H. Fu, A. Peng, T. Zhai, Y. Ma, F. Yuan, J. Yao, Adv. Mater. 21 (2009) 1636.
[13] B. Lv, Y. Hu, D. Wu, Y. Sun, Mater. Res. Bull. 44 (2009) 961.
[14] H.-M. Fan, J.-B. Yi, Y. Yang, K.-W. Kho, H.-R. Tan, Z.-X. Shen, J. Ding, X.-W. Sun, M.C. Olivo, Y.-P. Feng, ACSNano 3 (2009) 2798.
[15] X. Hu, J.C. Yu, J. Gong, Q. Li, G. Li, Adv. Mater. 19 (2007) 2324.
[16] M. Eltschka, M. Kläui, U. Rüdiger, T. Kasama, L. Cervera-Gontard, R.E. Dunin-Borkowski, F. Luo, L.J. Heyderman, C.-J. Jia, L.-D. Sun, C.-H. Yan, Appl. Phys. Lett. 92 (2008) 222508.
[17] B. Van Waeyenberge, A. Puzic, H. Stoll, K.W. Chou, T. Tyliszczak, R. Hertel, M. Fähnle, H. Brückl, K. Rott, G. Reiss, I. Neudecker, D. Weiss, C.H. Back, G. Schütz, Nature 444 (2006) 461.
[18] M. Gotić, G. Koščec, S. Musić, J. Mol. Struct. 924–926 (2009) 347.
[19] M. Ristić, S. Popović, S. Musić, Mater. Lett. 58 (2004) 2494.
[20] V. Barrón, J.L. Rendon, J. Torrent, C.J. Serna, Clays Clay Miner. 32 (1984) 475.
[21] J.L. Rendon, C.J. Serna, Clay Miner. 16 (1981) 375.
[22] C.J. Serna, J.L. Rendon, J.E. Iglesias, Spectrochim. Acta 38 (1982) 797.
[23] Y. Wang, A. Muramatsu, T. Sugimoto, Colloids Surf. A 134 (1998) 281.
[24] I. Chamritski, G. Burns, J. Phys. Chem. B 109 (2005) 4965.
[25] M. Blanchard, M. Lazzeri, F. Mauri, E. Balan, Am. Miner. 93 (2008) 1019.
[26] H.M. Fan, G.J. You, Y. Li, Z. Zheng, H.R. Tan, Z.X. Shen, S.H. Tang, Y.P. Feng, J. Phys. Chem. C 113 (2009) 9928.
[27] K. Kandori, Y. Aoki, A. Yasukawa, T. Ishikawa, J. Mater. Chem. 8 (1998) 2287.
[28] K. Kandori, A. Yasukawa, T. Ishikawa, Ind. Eng. Chem. Res. 39 (2000) 2635.
[29] K. Kandori, J. Sakai, T. Ishikawa, Phys. Chem. Chem. Phys. 2 (2000) 3293.
[30] S. Musić, A. Vertes, G.W. Simmons, I. Czako-Nagy, H. Leidheiser Jr., J. Colloid Interf. Sci. 85 (1982) 256.
[31] T.P. Almeida, M.W. Fay, Y. Zhu, P.D. Brown, Nanoscale (2010), doi:10.1039/c0nr00280a.
[32] T.P. Almeida, M.W. Fay, Y. Zhu, P.D. Brown, J. Phys. Chem. C 113 (2009) 18689.
[33] T.P. Almeida, M.W. Fay, Y. Zhu, P.D. Brown, Cryst. Eng. Commun. 12 (2010) 1700.